Three-Dimensional Electron Microscopy of Individual Biological Objects
Part II. Test Calculations

W. Hoppe, H. J. Schramm, M. Sturm, N. Hunsmann *, and J. Gaßmann

Max-Planck-Institut für Biochemie, Abteilung für Strukturforschung I, Martinsried bei München, West Germany

(Z. Naturforsch. **31 a**, 1370–1379 [1976]; received September 6, 1976)

In this second part of the paper the general conclusions of part I with regard to resolution and image point shape, variable boundaries of the projected three-dimensional body and origin definition have been tested by computer simulations. The influence of clutter and noise has been discussed.

Introduction

In the first part of this paper (part I) the general principles of three-dimensional electron microscopic reconstruction of individual molecular structures have been discussed. It has been shown that the restriction of the tilting angles, unavoidable in the case of extended specimens, necessarily leads to image points with certain distortions. These distortions are quite pronounced in the simple case of tilting around a single axis, but in future could be considerably reduced by a conical tilting scheme. For this technique, it is vital to determine the common origin of the projections, and so a new type of correlation function has been introduced. Of great importance is the fact that the significance of a three-dimensional structure is the same as for a two-dimensional image with the same radiation dose. This means that the discrimination in the third dimension does not require a higher electron dose. A significant three-dimensional structure can be reconstructed from insignificant two-dimensional projections. It is a happy coincidence that the common origin can be determined by correlation methods using insignificant images. For the proof of this statement see [1], which utilizes in another connection the significance of correlations of insignificant defined structures. If one wanted to define the common origin by marker points like in other fields of three-dimensional reconstruction (e. g. computerized tomography)[2] – only significant projections could be used. A minimal dose three-dimensional reconstruction would then be impossible. In this paper, calculations will be described which prove the reconstruction scheme on a test example, which resembles a real structure. Simple computer simulations have been done in the past on artificial models (like circular disks with sharp edges etc.) which have little relation to the electron microscopy in practice. We have also simulated the correlation method of origin definition and the effect of boundary conditions on the three-dimensional reconstruction.

Reprint requests to Prof. Dr. W. Hoppe, Max-Planck-Institut für Biochemie, Abteilung für Strukturforschung I, *D-8033 Martinsried bei München.*

* Present address of Dr. Hunsmann, Bayer AG, D-5090 Leverkusen.

Test Calculations

Our test structure consisted of a "carbon foil" constructed from tiny graphite crystallites (~ 7.5 Å diameter, ~ 6.5 Å thickness) arranged with random orientations in a random network. This structure had a calculated density, which was a factor of two lower than the density of a real carbon foil. This means that the "porosity" of the calculated structure was very high, because we did not apply minimum distance conditions between microcrystals. This deviation from real amorphous carbon is unimportant, as our aim is only to test our reconstruction scheme. At the top of the "foil" $Ta_6Br_{12}{}^{++}$-ions (Fig. 1 a) have been arranged in order to show the discrimination between heavy and light atoms.

For the next step – the calculation of projections – a "calculated" tilting axis within the specimen had to be determined and the extension of the projected image perpendicular to the tilt axis had to be defined. The size of the model foil (with two $Ta_6Br_{12}{}^{++}$-ions on the top) was kept small ($50 \times 50 \times 17$ Å) in order to avoid excessive calculation times. This size restriction increases the shape effects

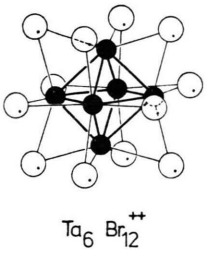

Fig. 1 a. Structure of the $Ta_6Br_{12}^{++}$-ion. Distance Ta—Ta= 2.9 Å, Ta—Br=2.6 Å.

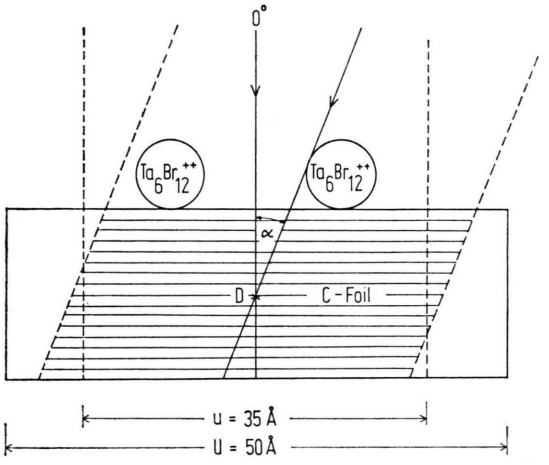

Fig. 1 b. Constructed "carbon foil" with heavy atom complexes to show discrimination of heavy and light atom in 3*D*-reconstruction. The total specimen dimensions, the reconstructed body and the position of the tilt axis *D* are given.

(see part I), which therefore should show up in the reconstruction.

Figure 1 b shows a schematical projection of the specimen along the *y*-axis (tilt axis direction). For the calculations, the position of the tilt axis *D* and the extension of the projection perpendicular to the tilt axis *u* had to be defined. It is evident that the axis *D* should be chosen within the specimen. An external position would produce shifted projections with only partial or even no overlap. The ideal position of the axis *D* (see Fig. 1 b) is in the middle of the foil. In this case no shifts of the foil projection will occur (Fig. 5, part I). The reconstruction size *u* must be smaller than the width *U* of the test specimen (in our case $U = 50$ Å). If one would assume $u > U$ the total (finite) specimen would be reconstructed with no cut difficulties. We have therefore chosen $u = 0.7\,U$ (in our case $u = 35$ Å). It follows from simple geometric arguments (see Fig. 1 b) that for a restricted tilted angle range up to $\sim 40^\circ$ the foil acts as an infinite specimen. For ranges $> 40^\circ$ the restricted size of the specimen does not give rise to the difficulties which would occur in the case of a real extended specimen. It is therefore possible to check the reconstruction scheme for the experimentally inaccessible case of $\alpha_{max} = \pm 90^\circ$. We explained in part I that the projection extension $u = u_0 \cos\alpha$ implies that the projected volume region S, which contributes to all projections, must be taken into account. Within region S all projections contain information for building up the image points in the reconstruction procedure. Using backprojection principles one can demonstrate that in the constant volume case ($u = u_0 \cos\alpha$) the region S (Fig. 2) is limited by both surface

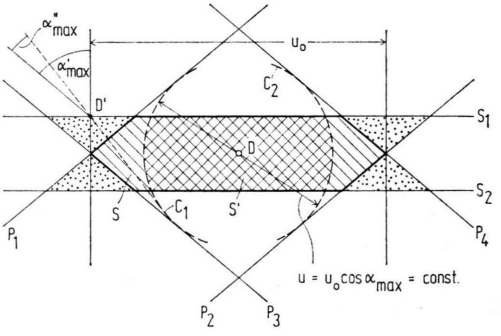

Fig. 2. Reconstruction of carbon foil regions with different contributions from the projections. The central part S′ is formed from all projections if constant dimension condition $u = u_0 \cos\alpha_{max} = \text{const}$ is used. The part S is reconstructed from all projections if the constant volume condition $u = u_0 \cos\alpha$ is applied. The dotted regions are reconstructed by only some of the projections. So for image point *D′* only projections with a tilting normal in the region α''_{max} will contribute.

planes s_1, s_2 of the specimen and by the projection planes p_1, p_2, p_3, p_4. (S = sum of the hatched and the cross-hatched regions in Figure 2.) If one uses the condition $u = \text{const}$ (which enlarges the volume of the projected support proportionally to $\cos\alpha$), the extension of the region S perpendicular to the tilt axis will be limited by cylindrical surfaces. In Fig. 2 we have demonstrated this by setting $u = \text{const} = u_0 \cos\alpha_{max}$. The cross-hatched region S′, limited by s_1, s_2, c_1, c_2 will contribute to all projections. Under these conditions S′ is smaller than S.

To understand the reconstruction in the regions outside S, it can be seen from Fig. 2 that these points will be imaged by backprojections with an-

gular ranges α'_{max}. The values α'_{max} are smaller than the angular range for points inside S. The size of α'_{max} and the orientation of the symmetry line $\alpha' = 0$ depend on the position of the image point. By d^*-weighting, the backprojected point figures will be converted into the real "points" with shapes and orientations depending on α'_{max} and $\alpha' = 0$ (see part I). As can be deduced from Fig. 9 and Fig. 10 in part I these image points become more and more elongated with decreasing α'_{max}. At the same time their weight (and electron statistical significance) will be reduced as the measured projections only partially contribute to these image points. Therefore the image fades out with increasing distance but retains the correct specimen structure with increasing image point distortions. The distorted image points and their clutter penetrate into the fully reconstructed region S (or S′) and influence its structure. Fortunately, the clutter around the image points is concentrated in the immediate neighbourhood of the points (see Fig. 9 and Fig. 10 in part I). Therefore, only relatively small clutter will occur inside the fully reconstructed region. It can therefore be predicted that the shape effects will not strongly influence the reconstruction. This is obviously of great importance for the reconstruction of cutouts of specimens on an unlimited supporting foil. The interesting point is that in the case $u =$ const the projections are limited by a cylinder of diameter u, whereas the reconstructed body is larger due to the reconstruction of regions outside S with $\alpha'_{max} < \alpha_{max}$. As the interpolation in all reconstruction schemes are based on the zero density outside the reconstructed body, the diameter of the reconstructed region should be chosen larger than the interesting region u (depending on the thickness of the foil and on α_{max}). In the case of negatively stained molecules the thickness of foil and negative stain might be considerably smaller than the thickness of the stained molecular structure. In this case the different projection cutouts could be neglected, especially if the structure at the border is of no interest. It is true that in the case $u = u_0 \cos\alpha$ (constant volume case), the volume of the regions which will be incompletely projected is considerably smaller than in the case $u =$ const. However, in the latter case the fully reconstructable body S′ has cylindrical symmetry and it fades out more smoothly than in the constant volume case. It is, therefore, difficult to predict whether the latter definition

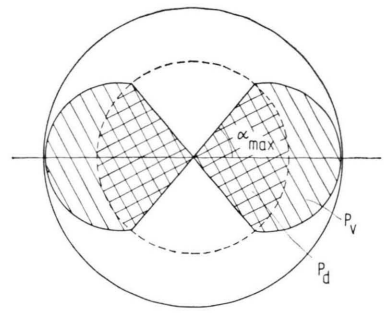

Fig. 3. Dependence of the width P of the projections (x-direction) from the tilt angle α for constant volume condition $u = u_0 \cos\alpha$ (P_V, hatched) and constant dimension condition $u = u_0 \cos\alpha_{max}$ (P_d).

really has considerable advantages. As already mentioned we reconstruct at present with $u =$ const.

In order to take into account these shape effects in our test calculations, a reconstruction diameter of 50 Å and a projection space diameter of 35 Å has been chosen (see Figure 3). Thus the reconstructed body will be completely circumscribed by the reconstruction region and the zero condition outside this region is valid to a good approximation.

Figure 4 a and Fig. 4 b show two projections of the model specimen at $\alpha = 0°$ and at $\alpha = 15°$. Note the identical size of the projections. Figure 4 c

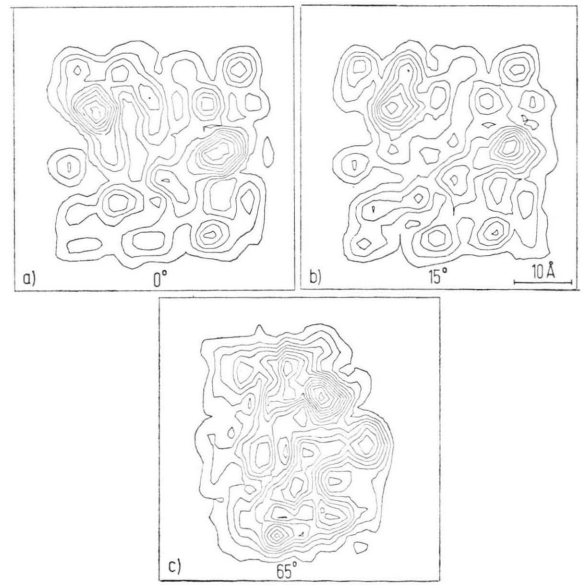

Fig. 4. Projections of the test structure at tilt angels $\alpha = 0°$, 15°, 65° (constant dimension condition $u = u_0 \cos\alpha_{max}$). Note the shortened projection at $\alpha = 65°$ due to the finite specimen extension (50 Å). Ideal image conditions for phase contrast (Zernike plate) assumed. Contrast ϱ_p defined in percents of I_0 ($\varrho_p = \Delta I / I_0$). Layer line distance = 0.02.

shows the projection at $\alpha = 65°$. The projection appears shortened in the x-direction, because for angles larger than 40° the body appears finite. This makes it possible to test the reconstruction up to $\alpha_{max} = \pm 90°$.

We report in the following, some characteristic results from these calculations. Figure 5 shows four

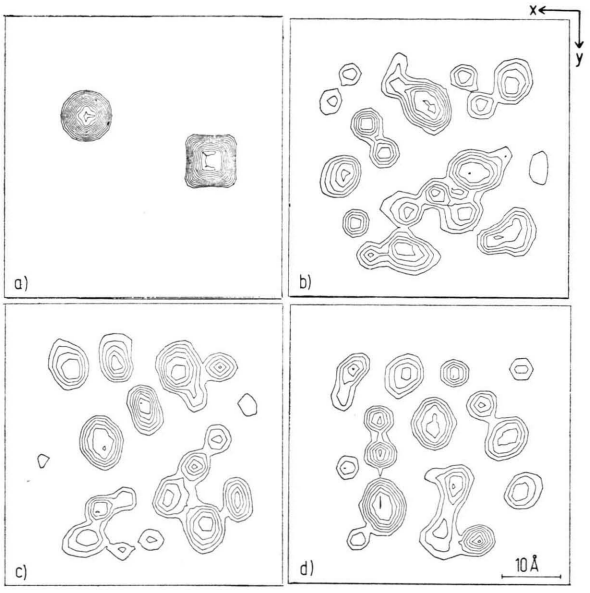

Fig. 5. Calculated densities of the test structure in four sections cut parallel to the surface of the "carbon foil" at 3.7 Å resolution. Position of the sections see Figure 13. Image function ϱ in Figures 5—15 defined in $Å^{-1}$. The integration of ϱ along a projection direction delivers ϱ_p. Layer line distance $\sim 1.4 \cdot 10^{-3}\ Å^{-1}$, only positive contour lines are drawn. The potential function in electron volts can be calculated from ϱ by multiplication with the constant $\pi \hbar^2/\lambda m_e$ (=647 eV Å). Note however, that only in the ideal case the potential function is accurate. In practice the phase contrast loss due to the real transfer functions leads to errors.

sections of the calculated (ideal) density function in this region at 3.7 Å-resolution (defined as the reciprocal space frequency limit). Only the region $(35 \times 35\ Å^2)$ [3] is shown. One of the sections intersects the $Ta_6Br_{12}^{++}$-ions, the others intersect the foil parallel to its surface. Figure 6 shows a reconstruction from 36 projections with an angular increment of 5 degrees. The common tilt axis corresponds to D in Figure 1b. The images are nearly identical, but note the enhanced maxima a – h in Fig. 6 near the edges, produced by the shape effects. As predicted, these effects are small in spite of the comparable dimensions of cutout and foil thickness.

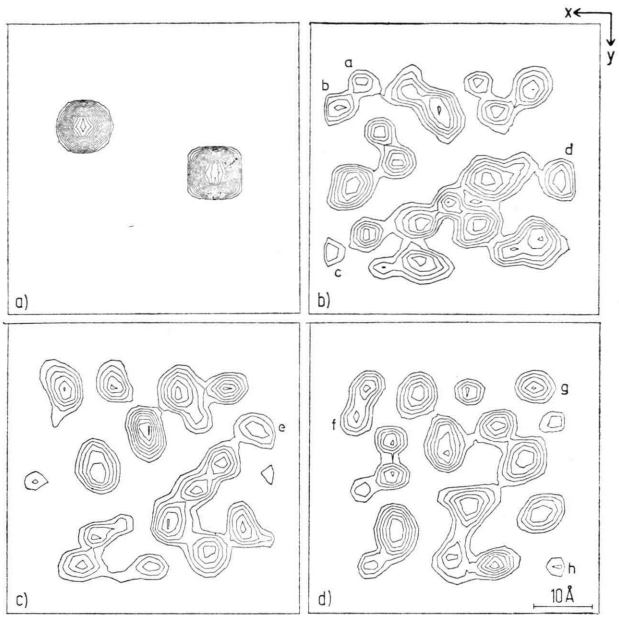

Fig. 6. Reconstructed densities of the same sections as Fig. 5 using 36 projections with 5° angular increments and ideal positioning with respect to the tilt axis. Very high correlation with the ideal density of Fig. 5 is apparent except in border regions.

We have presented in [4] (see also [5]) a simple relation for clutter-free interpolation

$$\pi/K = \Delta\alpha = 1/a\,d^* \qquad (1)$$

where K = number of projections, a = edge of a square, circumscribing the specimen, d^* = radius of the "clutter-free" reciprocal space, d = corresponding crystallographic resolution. It is obviously of interest, whether the Cormack-Smith reconstruction system in the version with the aliasing-free basic set of contributions leads to approximately the same resolution. Let us call the resolution determined by (1) the "marginal resolution". From (1) we calculate a marginal resolution of 4.36 Å for a reconstruction at 5° intervals inside a square of 50 Å diameter. In fact, the resolutions in Fig. 6 and in Fig. 5 ($d = 3.7$ Å) appear to be similar. But a calculation at intervals of 10° (18 projections) showed the same result, in spite of the low marginal resolution of $d = 8.72$ Å (Figure 7). Even a calculation at intervals of 20° (9 projections) shows at least the general appearance of the crystallite structure (Figure 8).

In order to understand these features we have analyzed the shape of the image point in Fig. 8,

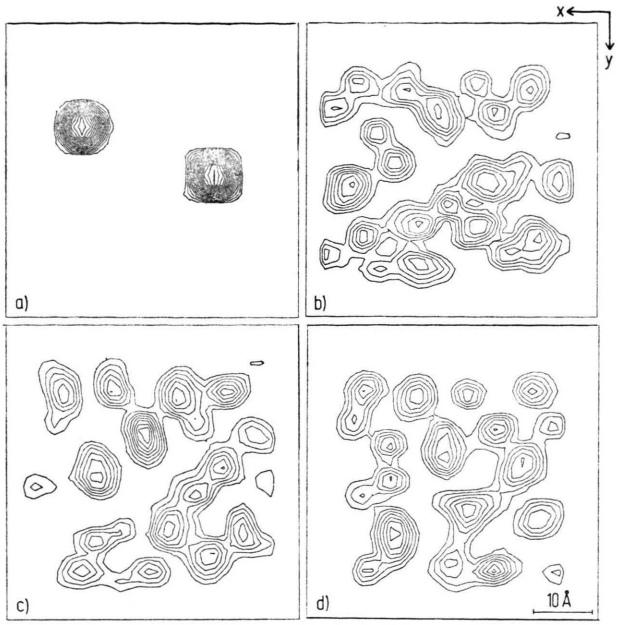

Fig. 7. Same as Fig. 6, but reconstructed from 18 projections with 10° increments. Although nominal resolution is lower by a factor of tho, very close similarity is apparent.

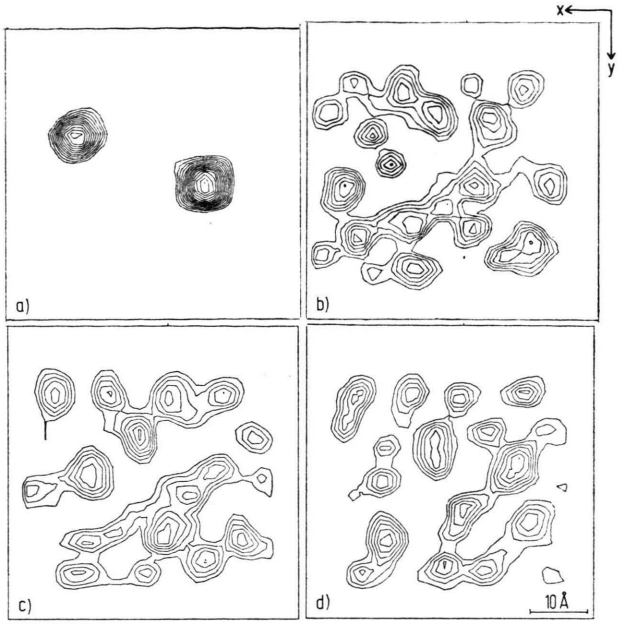

Fig. 9. Reconstructed densities similar to Fig. 6 including determination of common origin for all 36 projections.

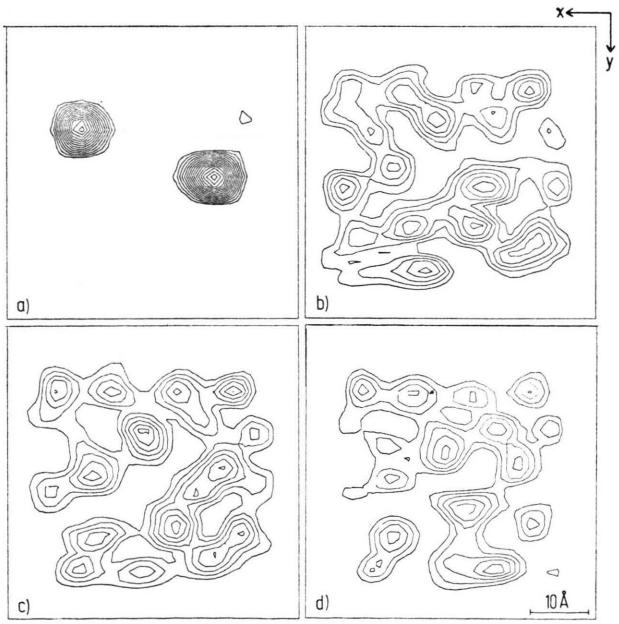

Fig. 8. Same sections as Fig. 6, but reconstructed from 9 projections with 20° increments. The general structure is still clearly visible.

part I, in more detail. The reconstruction range was $2R = 300$ Å, and the assumed resolution in the projections was 10 Å [6]. It can be shown that the image point function in Fig. 9 (part I) resembles the Bessel-function $J_1(x)/x$ (Fourier transform of a circular disc). This proves that Cormack-Smith reconstruction and Fourier inversion give similar image points (identical only for the central image point at $r = 0$). It is therefore possible to calculate from the diameter d_0 of the first zero line ($d_0 = 32$ Å), the corresponding virtual limit in diffraction space ($d_1^* = 1.22/32$ Å^{-1}) and a crystallographic resolution of $d_1 = d_1^{*-1} = 26$ Å. In order to use this result in connection with the image reconstructions in Fig. 6 and Fig. 7 we scale the above result to the range of $2R = 50$ Å. The resolution is then $26/6 = 4.30$ Å for an angular increment of 10°. As already suspected from the diagrams in Fig. 7, the actual resolution is better by a factor of two than the marginal resolution $d = 8.7$ Å. Further calculations have shown that this result is independent of the resolution in the projection from 6 Å to 20 Å (for $2R = 300$ Å). With a projection resolution greater than 25 Å the image point becomes broader. Note, that the shape is also quite independent of the resolution. If the image point moves from the centre to the border it becomes broader in azimuthal resolution, but not in the radial direction. For an image point, a distance of $0.5R$ from the centre, the widths are about 110% and 90% of the width of a central

image point (see Fig. 8, part I). This deformation will become much more pronounced, if the image point is near the boundary of the reconstructed cylinder. In Fig. 8 in part I the image point (distance from the centre $0.88\,R$) is elliptic with resolutions of about 40 Å (azimuthal) and about 10 Å (radial). Additional calculations show that there are side minima in the immediate neighbourhood of the peak, but there is also additional clutter at a distance of $\sim 100-200$ Å from the peak, with a ripple frequency which corresponds to the number of projections. In Fig. 6 and Fig. 7 border image points do not appear, as the three-dimensional body has been cut to 35 Å (distance of the border points from the centre $0.7\,R$). The enlargement of the reconstruction body has therefore the additional advantage of eliminating the strongly distorted image points near the border.

The next test calculations concern reconstructions including the determination of common origin. Figure 9 shows a reconstruction with $\alpha_{\max} = \pm 90°$, $\Delta\alpha = 5°$. The close similarity to Fig. 6 is evident. Calculations with similar results have been done for projections at $\Delta\alpha = 10°$. Note that the tilting axis determined by the correlation method moves somewhat upward with respect to D in Fig. 1 b (into the plane containing the centre of gravity of the squared structure). A detailed analysis of the errors has revealed an interesting effect[7]. Due to the condition $u = u_0$ the volume of the projected foil and therefore also its mass will be enlarged with increasing tilt angle. As the $Ta_6Br_{12}^{++}$-ions retain their mass, the centre of gravity of the squared structure moves downwards with increasing tilt. But the analysis has shown that this error can be neglected in the test case (and in the later reconstructions of fatty acid synthetase). It could be reduced by using the constant volume condition $u = u_0 \cos\alpha$ in the correlation determination, as the mass of the foil will be approximately constant. Other density inhomogenities within the specimen (especially at the boundaries) might lead to similar systematic errors. Some care is therefore necessary in defining the cutout.

In part I we have stressed the importance of two-dimensional reconstruction especially in cases where a strong defocusing occurs. Figure 10 demonstrates that the image of the structure will be completely destroyed, if for example the images have been taken with a defocusing of $\Delta z = 3000$ Å. A simple single image reconstruction (conversion of the nega-

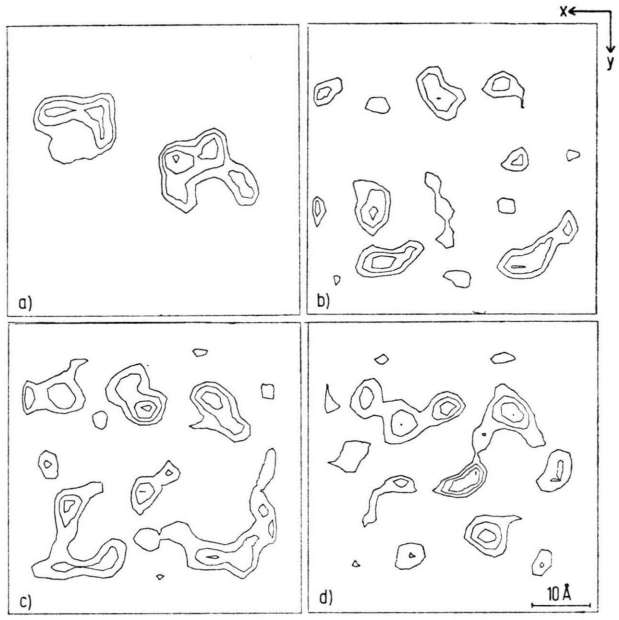

Fig. 10. Reconstructed densities similar to Fig. 6 without two-dimensional projection reconstruction. The assumed defocusing of 3000 Å completely destroys the image of the structure.

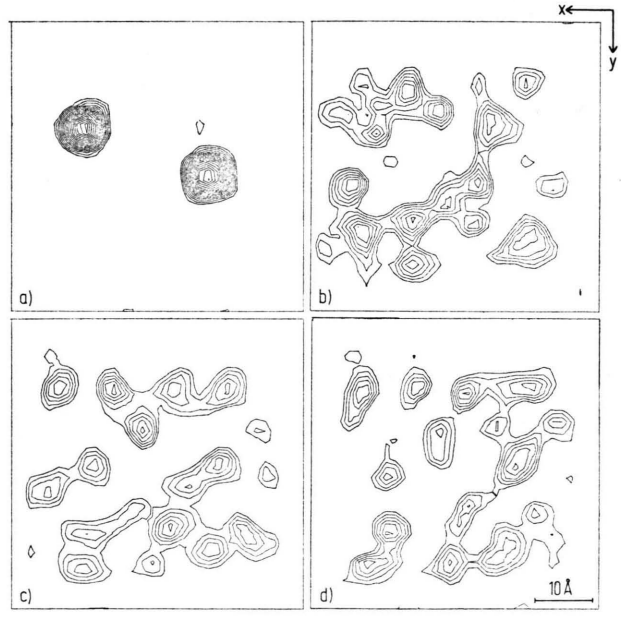

Fig. 11. Reconstructed densities similar to Figure 6. The assumed defocusing is 3000 Å. The correlation to the common origin and two-dimensional reconstruction for a defocusing of 2900 Å have been applied.

tive regions of spectral components) is sufficient to restore the image. Errors of ~ 100 Å in the determination of the defocusing had little influence on the structure in the test example (Figure 11).

The next point concerns the limited tilting range. Let us again start with a study of the image point which corresponds to a tilting series with $\alpha_{max} = \pm 45°$ (see Fig. 9 and Fig. 10 in part I). It is difficult to apply the usual optical resolving power criteria in this case. In the x-direction the sharpened image point (see Fig. 10 in part I) has strong negative side minima (see Fig. 9, part I). Their influence has been discussed in part I. However, an additional comment might be useful. The x^*-weighting (Fig. 10, part I) corresponds formally to the d^*-weighting, which is necessary for the conversion of the diffuse backprojection peaks to sharp image points (see part I). A weighting function, which reinforces the structure factors of higher order is a "sharpening function" in crystallography. If the profile of the object function density along x contains unsharp (positive) peaks with a slope decreasing as $1/x$ (x = distance from the peak) or slower, the decrease will become steeper but no negative regions will occur. If on the other hand the profile is already steep (e. g. sharp edge), negative artefact minima (as mentioned in part I) show up in the vicinity of the peaks. As Fig. 4 and Fig. 5 show, the graphite crystallites and the heavy atom ions appear at the restricted resolution of ~ 4 Å as unsharp peaks. Therefore in this case a sharpening without artefacts can be expected.

In the z-direction a broadening occurs (first zero line at 50 Å but no substantial rippling) which is due to the restricted range in Fourier space ($d^*_{max}/\sqrt{2}$ in the case of $\alpha_{max} = \pm 45°$, Fig. 9, part I). In order to get an estimate of the resolution in the z-direction we define the "point resolution distance" d_p by the known optical criterion of $\sim 75\%$ depression of the peak density in the connection line of both image points (in our case $d_p = 35$ Å). In the case of undistorted Bessel-type points at coherent illumination, the corresponding limit in Fourier space is given by $d_{cryst} = d_p/0.86$ (see for example [8]).

Defining, as above, a virtual crystallographic resolution d_{cryst} in the z-direction we get in our case $d_{cryst} = 41$ Å. This purely empirical definition will be supported by the fact that the image point density in the z-direction approximates to a Bessel-function $J_1(x)/x$. Table 1 contains the results of our estimates for our two cases $2R = 50$ Å and $2R = 300$ Å.

Table 1. Reconstruction resolutions (in Å) at 10° angular intervals.

cylinder diameter 50 Å		cylinder diameter 300 Å	
full range	45°-range	full range	45°-range
x-direction 4.4 (3.8)	[3.5]	26 (23)	[21]
z-direction 4.4 (3.8)	6.8 (5.9)	26 (23)	41 (35)

The values in the brackets are the coherent point resolutions in the x-direction. The resolution in the y-direction (direction of the tilting axis) will not be influenced by the tilting range. It corresponds simply to the projection resolution in the y-direction.

Figure 12 shows a test reconstruction with $\alpha_{max} = -45° \rightarrow +40°$, $\Delta\alpha = 5°$. By comparison with Fig. 6 it can be recognized that the general features

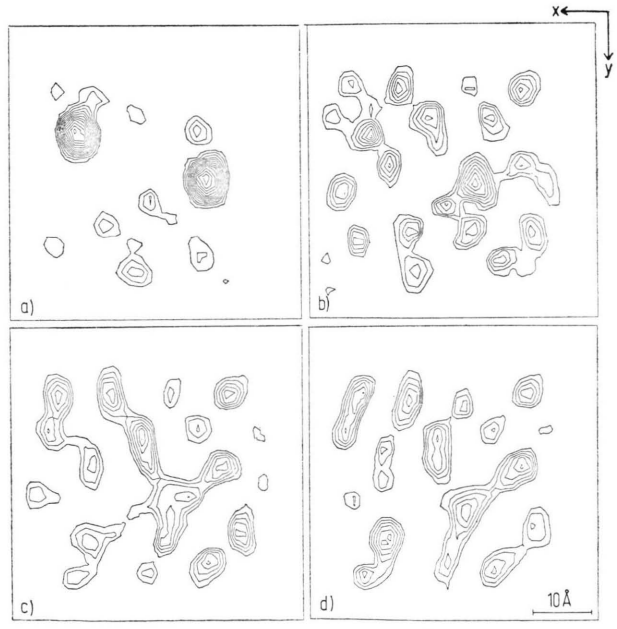

Fig. 12. Reconstructed densities similar to Fig. 6, from 18 projections with limited tilt range ($\alpha_{max} = -45° \rightarrow +40°$) and 5° angular increments. The correlation to the common origin and two-dimensional reconstruction have been applied. The general structure is still recognizable.

are retained. But the peaks representing the microcrystals in the foil appear – as predicted above – sharper (narrower) in the x-direction (see also the $Ta_6Br_{12}^{++}$-ions). As this sharpening is restricted to the neighbourhood of the peaks its influence will

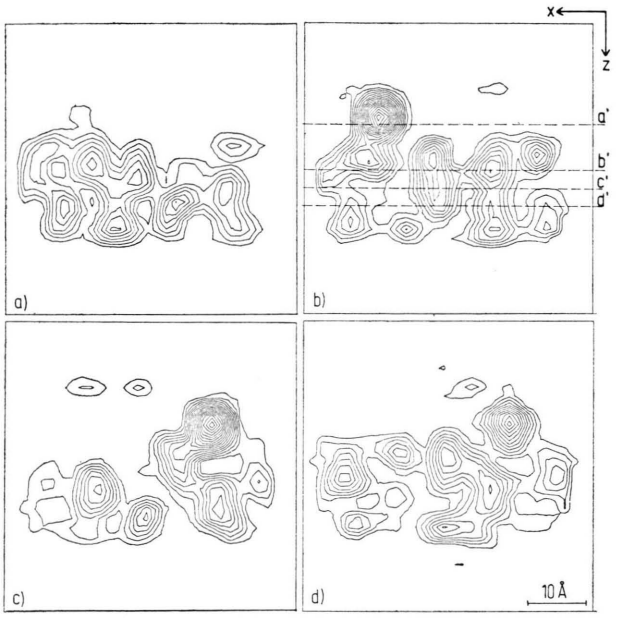

Fig. 13. Reconstructed densities perpendicular to foil surface and tilt axis from 18 projections in full tilting range and angular increments of 10°. a′, b′, c′ and d′ show the position of the sections a, b, c and d in Figs. 5–12.

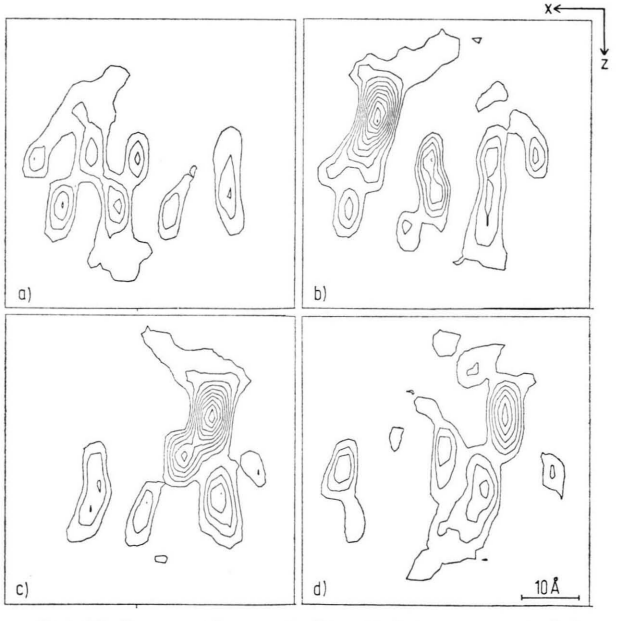

Fig. 14. Same sections as in Fig. 13, but reconstructed from 9 projections in a restricted tilt range ($\alpha_{max} = \pm 40°$) and with large increments (10°). The general appearance especially in the heavy atom regions is still present.

not propagate into other image regions. But obviously some care is necessary in drawing quantitative conclusions about shapes, sizes and weights.

Virtually the same results will be found, if one replaces $\Delta\alpha = 5°$ by $\Delta\alpha = 10°$ due to the cut-off of $d^*_{max} = 1/3.8$ Å in the "experimental data" (see also Table 1). Figure 12 a demonstrates the reduced resolution perpendicular to the image plane. In the image plane of the $Ta_6Br_{12}^{++}$-ions structural features of the supporting foil can be recognized. In an even more impressive way the elongation of the peaks in the z-direction and their contraction in the x-direction are demonstrated in Fig. 13 and Fig. 14, which compare x, z-sections having $\alpha_{max} = \pm 90°$, with sections having $\alpha_{max} = \pm 40°$ ($\Delta\alpha = 10°$ for both). Even in these distorted sections the main features of the structure can be recognized.

The Influence of Noise

Clutter (background around the image points) and noise (e. g. electron shot noise) both contribute to the distortion of an image. But their influence is basically different. Clutter also appears with "infinetely" accurate data, whereas noise then disappears completely. A reconstruction scheme which is quite clutter-free can lead to a detrimental noise amplification, which might entirely obscure the reconstructed structure even with very good experimental data. Therefore, it is necessary to study the used reconstruction scheme with respect to amplification of noise. Any reconstruction scheme converts – using some type of redundancies in the data – a set of measured data ψ' into a set of reconstructed data ψ which corresponds to the structure (distorted by a reasonable amount of clutter). In principle it does not matter, whether these redundancies are defined in real or reciprocal space. If for example ψ' is an experimental set of Fourier coefficients then ψ is the Fourier set necessary for the synthesis of the structure. By variation of the coefficients of ψ it can be checked, which coefficients are ill-defined. If large variations of these coefficients lead to small changes of ψ' then these coefficients cannot be recovered in the presence of noise as the ψ' variations due to noise are of similar order of magnitude. A simple two-dimensional example is the reconstruction of Fourier coefficients near the nodes of the transfer function. A three-dimensional example is the retrieval of coefficients in the blind region (restricted tilting angle) by Whittaker-Shannon "extrapolation" (see part I). The coefficients in this region have only little in-

fluence on ψ' [9]. Their retrieval in practice is therefore impossible. Interpolation schemes, which recover values of ψ more or less from the immediate neighbourhood of the corresponding ψ'-values (e. g. the generation of the missing projections in the Cormack-Smith reconstruction) are less liable to noise amplification. We have studied the influence of noise on our test calculations by addition of a certain amount of white noise to the projection data. For the discrimination of noise from clutter, the reconstructions have to be compared with the corresponding reconstructions with noise. Figure 15

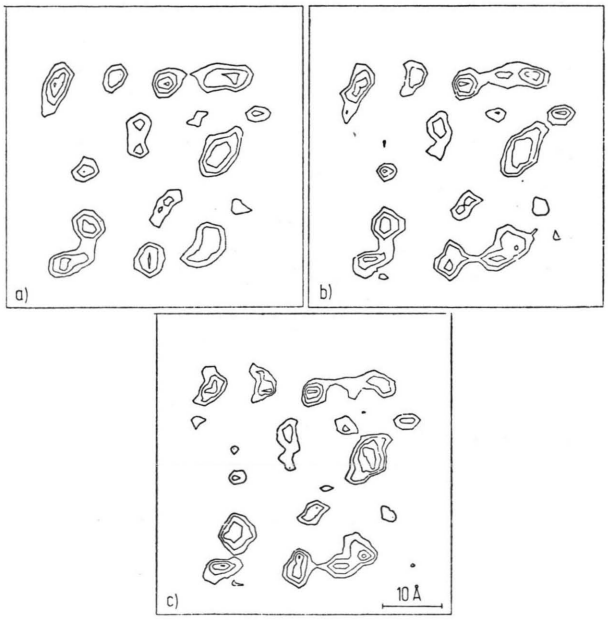

Fig. 15. Like Fig. 11 d, but calculated with various amounts of noise (see text). Only upper positive layer lines of ϱ are drawn.

shows some results demonstrated on the section which is imaged in Figure 11 d. For easier comparison only the upper contour lines have been drawn. Figure 15 a shows a reconstruction with 5% noise (with respect to the averaged projection density differences) assuming a reconstruction at $\Delta z = 3000$ Å (marginal resolution definition $\Delta\alpha = 5°$, $\alpha_{max} = \pm 90°$) calculated with a filter function corresponding to $z = 2900$ Å (as in Figure 11). The comparison with the zero noise reconstruction (Fig. 11 d) shows as expected only very little differences. Figure 15 b calculated with 10% noise (and calculations with further noise enhancement) show the increasing influence of noise. Of considerable interest is the reconstruction in Fig. 15 c, calculated like Fig. 15 b with 10% noise but at angular intervals of $\Delta\alpha = 10°$. The noise is greater than in Fig. 15 b, but smaller than in calculations with 20% noise, $\Delta\alpha = 5°$ (not shown). One could therefore suspect that a certain noise amplification is connected with the reduction of the number of projections. However, such a conclusion does not take into account that the error level in a three-dimensional reconstruction will be defined by the averaged noise level in all measured projections (corresponding in the case of electron shot noise to the total dose of the primary beam [10]). As the number of projections has been halved, the noise in Fig. 15 c should correspond to a noise of $\sqrt{2} \cdot 10\% \sim 14\%$ in the projections of a reconstruction with $\Delta\alpha = 5°$, thus explaining the noise increase in Figure 15 c. Klug and Crowther [11–13] have derived by a Fourier-Bessel analysis a noise amplification free resolution limit defined by

$$d^*_{max} = (K + C)/\pi D \qquad (2)$$

(C is a constant, typically about 6) which in our case would be only a factor 1.3 (instead of ~ 2) higher than the marginal resolution (1). We found that the noise enhancement claimed by Klug and Crowther for higher resolutions corresponds exactly to the reduction of experimental information discussed above [14]. With respect to the existing experimental technique, the reduction of the number of projections for a noise amplification free reconstruction is obviously of great practical interest. Note, however, that – as also shown in [11] – the clutter – especially the distortion of the image points near the edges (see Fig. 10 in part I) – decreases with the number of projections. In the case of the marginal resolution (1) this distortion disappears.

Another comment concerns the "noise" due to radiation damage. It is obvious that quasi-simultaneous recording (n-fold repetition of the tilting cycle) minimizes the influence of this type of noise. Each exposure is averaged over the integral exposure time t_0. Let us describe a radiation defect by an local specimen feature appearing (or disappearing) at a time t_1 between zero and t_0. In a quasi-simultaneous reconstruction it will be imaged in exactly the same way as the stable structure, however, with a reduced weight t_1/t_0 (disappearing) or $t_0 - t/t_0$ (appearing). Figure 16 demonstrates the case of the one-cycle reconstructions used in our experimental

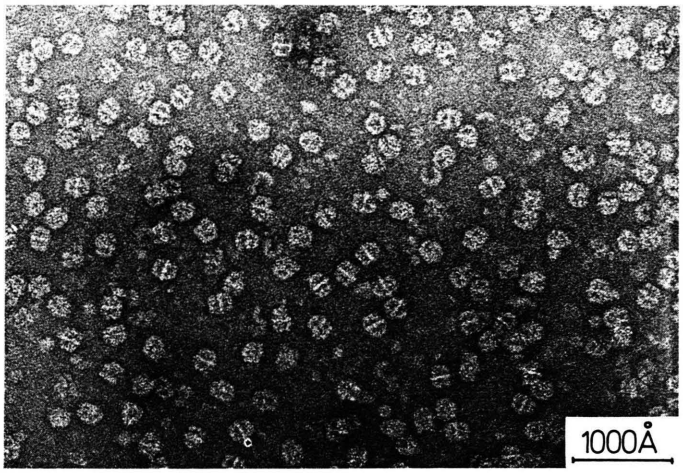

Fig. 1. General appearance of FAS-molecules in high dose images.

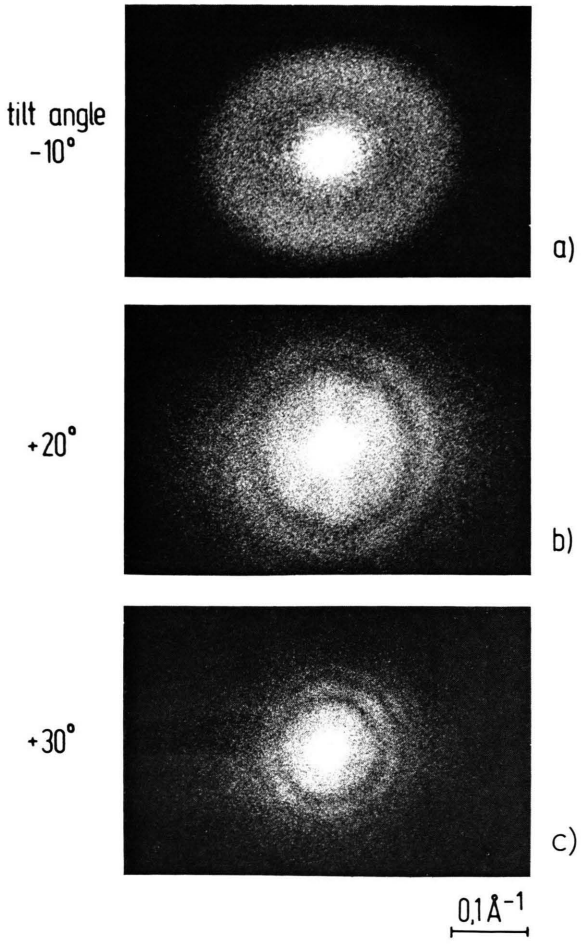

Fig. 3 a–c. Light diffractograms of projections from tilt series S 168-1 (Figure 2). The diffractograms show clearly the need for two-dimensional reconstruction of the individual projection. This was also indicated by the different focusing of the images in Figure 2 a–2 d.

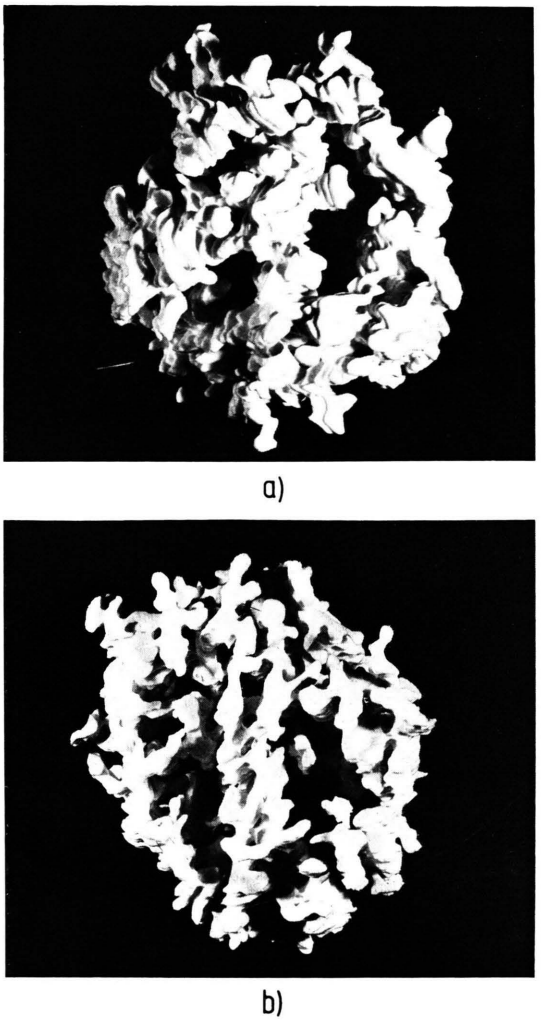

Fig. 16. Styropor models of the molecules S 168-1-II (a) and S 168-1-III (b) seen parallel to the central wall.